



# The Application of Electron Backscatter Diffraction on Halide Perovskite Materials

Hongyu Sun, Gede W.P. Adhyaksa, and Erik C. Garnett\*

Recently, the application of electron backscatter diffraction (EBSD) in halide perovskites has enabled the correlation of the micro-structural arrangement of polycrystalline grains with other properties (optical, electrical, mechanical, and chemical) in a “pixel-by-pixel” approach. Most studies so far have used an ultra-sensitive electron beam detector that has sensitivity thousands of times higher than a traditional scintillator screen and charge coupled device camera, enabling much lower beam currents. An alternative approach has been the use of low vacuum measurement conditions to avoid charge buildup that leads to damage. This review focuses on introducing the classical EBSD technique to the halide perovskite community, where it has been highly underutilized due to beam-induced damage in these relatively unstable materials. Recent research is used to dispel some common misconceptions about grain boundaries in halide perovskites and highlight what has been learned by comparing and correlating EBSD with other techniques. Additionally, the remaining limitations, development challenges, and future of the EBSD technique for halide perovskites are discussed. Successful utilization of the EBSD technique as a common characterization tool in the halide perovskite community will enable scientists and engineers to develop maps of cross correlated properties, helping to unlock the full potential of this complex material system.

## 1. Introduction

Although a very old class of materials, first discovered over a century ago,<sup>[1]</sup> the halide perovskite family has garnered renewed attention in the past decade. This renewed interest has been spurred by their very simple preparation by solution processing, their facile bandgap tuning, and particularly their ability to demonstrate outstanding optoelectronic properties with relatively little synthetic optimization.<sup>[2–7]</sup> In spite of the large body of work focusing on characterization of optoelectronic properties and device performance, many fundamental questions about the materials remain relatively unexplored,

H. Sun, Dr. G. W. P. Adhyaksa, Prof. E. C. Garnett

Center for Nanophotonics

AMOLF

Science Park 104, Amsterdam 1098 XG, The Netherlands

E-mail: e.garnett@amolf.nl

 The ORCID identification number(s) for the author(s) of this article can be found under <https://doi.org/10.1002/aenm.202000364>.

© 2020 The Authors. Published by WILEY-VCH Verlag GmbH & Co. KGaA, Weinheim. This is an open access article under the terms of the Creative Commons Attribution License, which permits use, distribution and reproduction in any medium, provided the original work is properly cited.

DOI: 10.1002/aenm.202000364

including the formation and behavior of grain boundaries, the importance of crystallographic orientation and phase separation, as well as the impact of local strain on optoelectronic properties. These questions are usually addressed using techniques that can measure crystallographic properties, such as X-ray and electron diffraction as well as lattice-resolved transmission electron microscopy (TEM).

TEM and X-ray-based crystallographic techniques each have their advantages and disadvantages. Using TEM to study crystallinity of thin-films requires extensive sample preparation which is both time consuming and always has the risk of altering the nature of the sample. The material damage, for example, during the preparation of thin lamellae by focused ion beam milling, is especially a concern for delicate materials such as the halide perovskites.<sup>[8–14]</sup> Due to the long sample preparation time and the local nature of TEM analysis, typically it is only practical to examine a small number of sites,

prohibiting access to information about sample heterogeneity, grain size distribution, grain boundary properties, or grain orientation effects on a scale beyond a few microns. The destructive nature of the technique also makes it difficult or impossible to correlate crystallographic information directly with optoelectronic properties. At the other end of the spectrum, X-ray diffraction (XRD) is usually non-destructive and can easily measure crystallographic properties of large area thin-films, including the average grain size, for example, from peak broadening. However, grain size estimates are complicated by effects of strain and grain shape. Additionally, standard XRD cannot provide any local (e.g., 1  $\mu\text{m}$  scale or smaller) measurements, which are required for understanding grain size distribution as well as for correlating specific grain orientations or special grain boundaries with the resulting optical or electrical properties. Since local crystallographic properties require the use of nano-diffraction at a synchrotron,<sup>[15,16]</sup> XRD with nanoscale resolution is less commonly used to relate local crystallographic and optoelectronic properties.

For thin-film samples and correlative measurements, electron backscatter diffraction (EBSD) is the technique of choice for determining crystallographic properties.<sup>[17–22]</sup> Traditional EBSD setups use a phosphor screen and camera to visualize electrons diffracted from the surface of a crystal or thin-film.<sup>[23,24]</sup> The symmetry of the diffraction pattern can provide

information on the crystal phase, crystallographic orientation, and even local strain. The most common electron source is the electron gun inside a scanning electron microscope (SEM), which immediately provides crystallographic mapping capabilities with sub-micron spatial resolution. Since most thin-film materials can be imaged in the SEM without significant beam damage, EBSD is typically considered a non-destructive technique. However, due to the very sensitive nature of halide perovskites, they are often damaged or even destroyed under standard EBSD imaging conditions, such that the technique has largely been neglected by the community. However, recent breakthroughs in detectors as well as the implementation of low-vacuum measurements have enabled much lower beam currents or higher beam resistance that are in some cases compatible with EBSD mapping of halide perovskite thin films.<sup>[25–28]</sup> The goal of this article is to introduce the EBSD technique to the halide perovskite community, highlight what has been done so far with this class of materials, and lay out some of the most exciting directions to explore with EBSD moving forward.

## 2. Historical Milestones of EBSD

In 1928, Nishikawa and Kikuchi<sup>[29]</sup> found pairs of diffraction lines (bands) on a photographic plate when a crystal was exposed to a monochromatic beam of cathode rays at 6° grazing incidence (Figure 1a). These lines later became known as “Kikuchi” lines. In 1935, Laue<sup>[30]</sup> thought that the Kikuchi lines originated from electrons inelastically backscattered by Bragg planes from an excitation volume buried inside the crystal. In 1954, Pashley et al.<sup>[31]</sup> built a chamber which could repeat Kikuchi’s experiment but with a wider grazing angle range from 2° to 164°. Kikuchi lines were found to be sharpest near 30° grazing angle. By implementing this optimized geometry, they found these lines could provide more information related to crystal orientation (Figure 1b). In the 1970’s, along with a rapid development of the modern SEM, came the first attempts at “scanning” crystal orientation.<sup>[32]</sup> In 1986, Dingley et al.<sup>[33]</sup> started popularizing a technique which overlapped the observed Kikuchi patterns with simulated patterns of the expected crystal orientations. This began the period where computer-based indexing is used to enable mapping crystallographic orientation on a larger scale and in real-time. In 1992, Wright et al.<sup>[34]</sup> after modifying an algorithm from Burns et al.,<sup>[35]</sup> developed the first algorithm to speed up the indexing procedure, including image quality, band detection, correlation, and orientation calculation. This represents the beginning of automatic EBSD analysis using a big dataset. The charge-coupled device (CCD) invented by Smith and Boyle (2009 Nobel Prize in Physics) transformed image sensor technology, including EBSD’s camera as a standard microstructural characterization tool in many fields of materials science and engineering.<sup>[36]</sup> Figure 1c–i shows just a small subset of the materials systems that have been analyzed with EBSD, including metal alloys,<sup>[37]</sup> stainless steels,<sup>[38]</sup> biological composites,<sup>[39]</sup> III-V epitaxial layers on individual nanoparticle,<sup>[40]</sup> micro trenches,<sup>[41]</sup> nanowire arrays,<sup>[42]</sup> and even the surface of ice.<sup>[43]</sup>



zation of halide perovskite materials.

**Hongyu Sun** is a Ph.D. researcher working at AMOLF, Amsterdam. He works in the Nanoscale Solar Cells group under the supervision of Prof. Dr. Erik Garnett. He obtained his B.Sc. (2016) from Beijing Institute of Technology and M.Sc. (2018) from University of Amsterdam. His research expertise is in nanofabrication for solar cells and characteri-



detector EBSD for microstructural analysis of halide perovskites. His is currently appointed as a research academic at the School of Chemistry and Molecular Bioscience at the University of Queensland, Australia.

**Gede Adhyaksa** received B.Eng. (cum laude) in engineering physics from the Institute Technology of Bandung (2008), and Ph.D. in physics from the University of Amsterdam (2018). His Ph.D. research was carried out at AMOLF Institute, Amsterdam, The Netherlands, where he pioneered the application of a direct electron



Peidong Yang. He conducted postdoctoral work at Stanford with Prof. Mark Brongersma, Yi Cui, and Mike McGehee before joining AMOLF in 2012.

**Erik Garnett** is a tenured group leader at AMOLF in Amsterdam and Professor of Nanoscale Photovoltaics at the University of Amsterdam. He received his B.S. in chemistry from the University of Illinois, Urbana-Champaign (2004), and his Ph.D. in chemistry from the University of California, Berkeley (2009) under the supervision of Prof.

As an advanced thin film characterization technology, EBSD has been widely employed to study polycrystalline films used as the absorber material for photovoltaics including CIGS,<sup>[44,45]</sup> CdTe,<sup>[46,47]</sup> CZTS,<sup>[48,49]</sup> and Si.<sup>[50]</sup> EBSD has been particularly valuable when used in combination with other techniques such as electron beam induced current (EBIC), atom probe tomography (APT), and cathodoluminescence (CL) in order to understand the connection between grain boundary properties and charge carrier separation, chemical defect segregation,

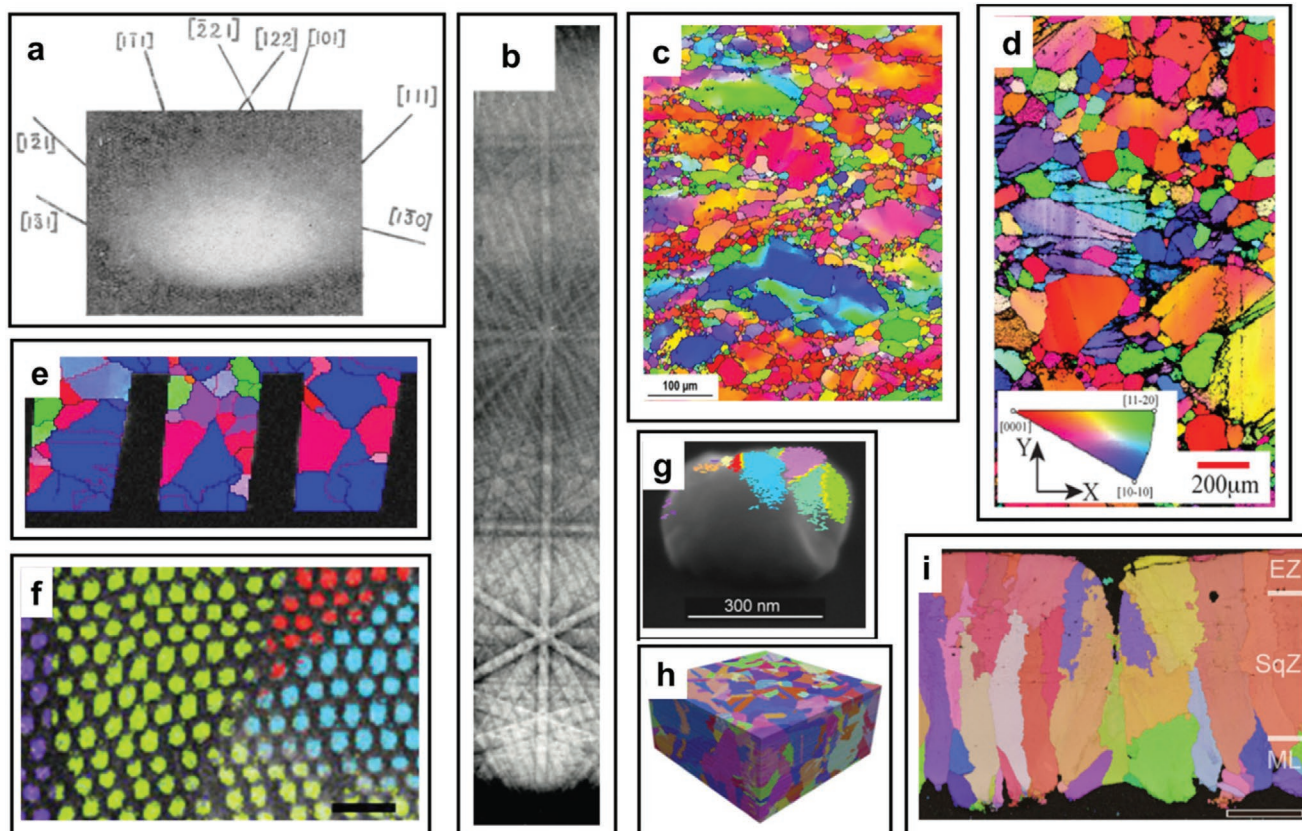


**Figure 1.** a) First observation of pairs of diffraction lines (known as Kikuchi lines). Reproduced with permission.<sup>[29]</sup> Copyright 1928, Nature Publishing group. b) Optimized Kikuchi lines at high grazing angles. Reproduced with permission.<sup>[31]</sup> Copyright 1954, Royal Society, and examples of EBSD maps on various subset of material systems. c) Mg-Zn-Cr alloy. Reproduced with permission.<sup>[37]</sup> Copyright 2018, Elsevier, d) surface of ice. Reproduced with permission.<sup>[43]</sup> Copyright 2015, Wiley, e) Cu trench microstructures. Reproduced with permission.<sup>[41]</sup> Copyright 2017, Elsevier, f) Si nanowires. Reproduced with permission.<sup>[42]</sup> Copyright 2012, American Chemical Society. g) GaAs on individual Si nanoparticle. Reproduced with permission.<sup>[40]</sup> Copyright 2017, IOP Publishing, h) 3D map on 316L stainless steels. Reproduced with permission.<sup>[38]</sup> Copyright 2018, Cambridge University Press, and i) eggshells. Reproduced with permission.<sup>[39]</sup> Copyright 2019, Wiley.

and non-radiative recombination, respectively. These correlated techniques have shown that grain boundaries can have very different effects, both positive and negative, depending on the type of semiconductor, the chemical impurities present, and the nature (e.g., crystallographic orientation or angular mismatch) of the grain boundary. For example, in silicon, high angle and random grain boundaries are the most detrimental, at least in part due to their propensity to getter metal impurities, while low-angle and coherent twin grain boundaries have relatively little impact on performance.<sup>[50]</sup> In CdTe, the opposite is true; the same defect accumulation allows for random and high-angle grain boundaries to provide channels with inverted polarity, which leads to drastically improved carrier collection<sup>[47]</sup> (Figure 2). Low-angle and twin boundaries on the other hand lead to enhanced carrier recombination in CdTe. CIGS shares some characteristics with both Si and CdTe; twin boundaries appear to be nearly inert (as in Si), but other random grain boundaries provide greatly enhanced carrier collection due to local polarity inversion (as in CdTe<sup>[51]</sup>). These few examples show the power of EBSD, especially in combination with other techniques like EBIC and CL that are readily available in the

SEM as well, to provide a deeper understanding of the underlying mechanisms behind the empirically observed positive and negative effects of crystallographic defects in photovoltaic materials.

### 3. Working Principle of EBSD

#### 3.1. Setup

A standard EBSD measurement is carried out inside the SEM chamber using a direct electron detector or traditional phosphor screen and camera (Figure 3a,b). Geometrically, the sample is mounted at a 70° tilt relative to the orthogonal axis of the incoming electron beam. At this high tilt angle, incident electrons travel through a longer pathway in the near-surface region, increasing the scattering volume.<sup>[52]</sup> As shown in Figure 3a, scattering events only happen in the near-surface region. The depth, size, and shape of the scattering volume mainly depend on the accelerating voltage of the incident beam and the average atomic number (Z) of the

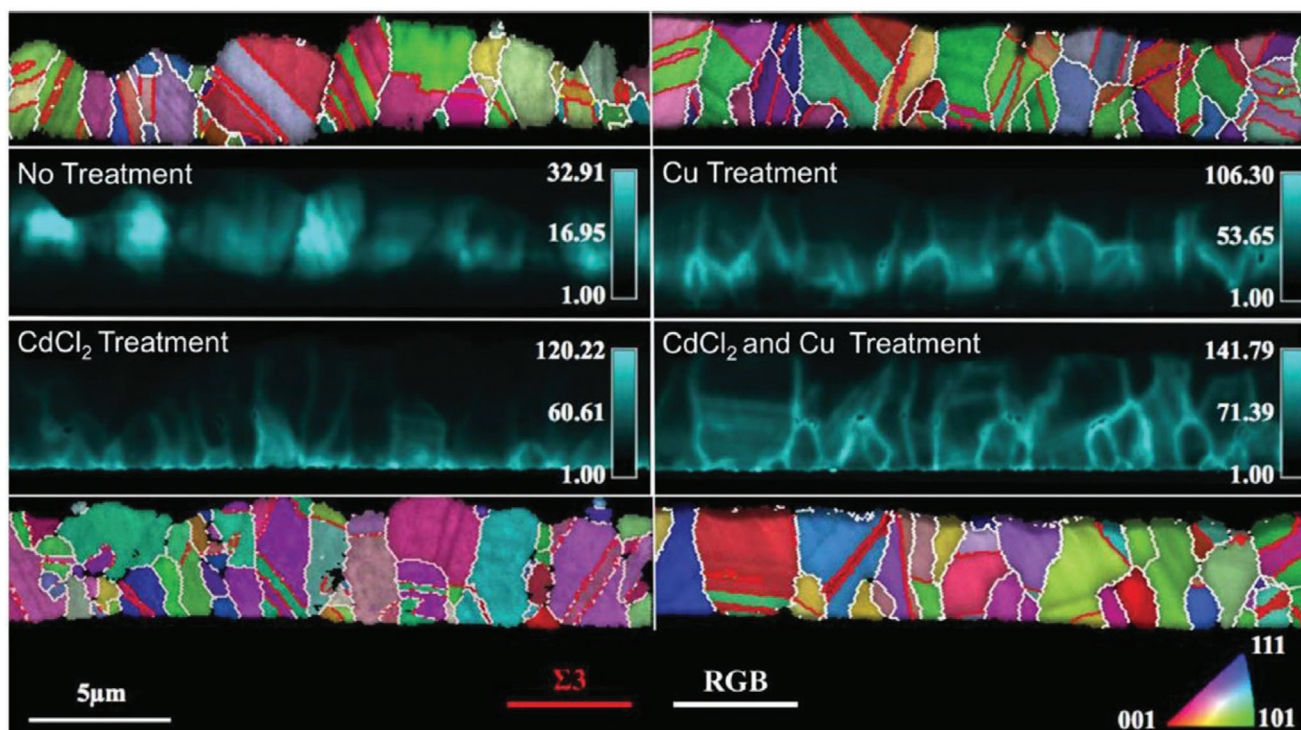


**Figure 2.** EBSD map on CdTe film with no treatment, Cu treatment, CdCl<sub>2</sub> treatment, and two treatments together. Σ3 (in red) are coherent twin grain boundaries, while RGB (in white) are random grain boundaries. The corresponding EBIC maps are shown in the middle. Reproduced with permission.<sup>[47]</sup> Copyright 2014, Wiley.

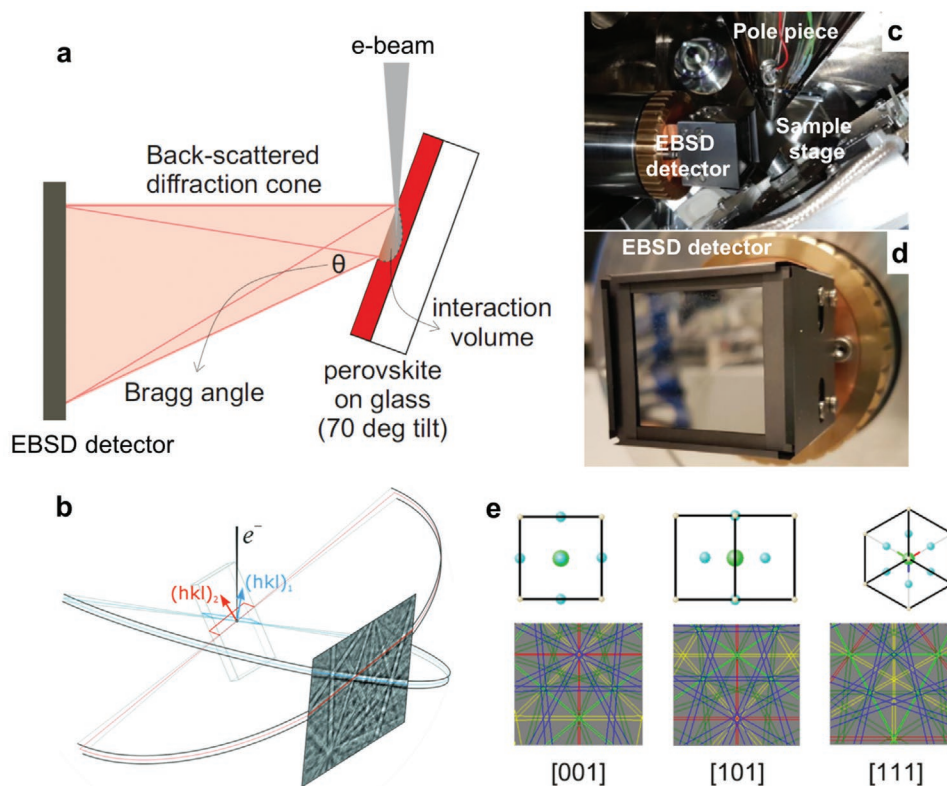


**Figure 3.** a) Schematic of EBSD setup. Reproduced with permission.<sup>[25]</sup> Copyright 2018, Wiley; b) formation of Kikuchi patterns explained by Kossel cones. Reproduced with permission.<sup>[10]</sup> Copyright 2015, International Union of Crystallography; c) example of EBSD setup inside SEM chamber; d) photograph of direct electron detector used for EBSD mapping in halide perovskites; e) simulated symmetry patterns for CH<sub>3</sub>NH<sub>3</sub>PbBr<sub>3</sub> perovskites at different crystal orientations.

sample. Probing depth is typically on the order of 100 nm, but a detailed simulation providing information about the size and shape of the probing volume can be carried out using Monte Carlo simulations, for example, using the popular CASINO software package.<sup>[25]</sup> Current commercial EBSD systems that use a phosphor screen and camera typically require relatively high accelerating voltages (e.g., 15–30 kV), which lead to larger excitation volumes, reducing spatial resolution and increasing the probing depth. The direct detector or phosphor screen is placed very close to the sample and can image the backscattered electrons escaping from the sample at specific Bragg angles, enabling identification of local crystal orientation (Figure 3c). The diffraction patterns that form, usually called Kikuchi patterns, resemble those expected for a point source of electrons located just beneath the sample surface; diffraction by lattice planes leads to a series of intersecting bands known as Kikuchi lines (Figure 3d). The Kikuchi patterns very much resemble those seen in TEM electron diffraction when imaging samples thick enough to exhibit multiple electron scattering. Just as in TEM electron diffraction, the crossing points of Kikuchi bands correspond to zone axes of the crystal—special high symmetry directions of the crystal. Since the Kikuchi bands correspond to lattice planes, the angles between the bands can be used to identify the crystal orientation (Figure 3e).<sup>[53]</sup> Scanning the beam across the sample surface allows patterns to be collected pixel-by-pixel, while comparison with simulated patterns enables indexing, ultimately leading to a microstructural map of the sample that includes information about crystal orientation, phase, strain, and grain boundaries.<sup>[24,54–58]</sup>

### 3.2. Sample Preparation

Successful EBSD always starts with sample preparation. The sample surface should be sufficiently smooth, with no debris or residual particles. Removing debris and residual particles sitting on top of the sample surface is necessary to avoid shadowing effects that may block the projection of Kikuchi patterns onto the screen. Any roughness can also decrease pattern clarity. In general, smooth surfaces can be obtained by mechanical, chemical, electro-polishing, ion-milling, or even plasma etching.<sup>[59]</sup> Unfortunately, most of these traditional smoothing techniques cannot be used for halide perovskite thin-films because of the soft and unstable nature of the materials under the mechanical, chemical, ion, and plasma etching stresses normally used. The complex halide perovskite compositions developed more recently that show greatly improved stability under solar cell operation, such as triple cation, mixed anion, and alkali doped materials, so far have not been studied with EBSD, so it is not known if they will have the same preparation challenges. However, there has been one example of the more stable (under the electron beam), fully inorganic CsPbBr<sub>3</sub> wafers cut from an ingot and polished using traditional methods, which led to a surface with sufficiently high quality to do EBSD mapping.<sup>[60]</sup> Recently, CH<sub>3</sub>NH<sub>3</sub>PbBr<sub>3</sub> perovskite samples with surface roughness up to 20 nm could be successfully mapped even without sample polishing.<sup>[25]</sup> Perhaps, the heavy lead and halide atoms that lead to large electron backscatter cross sections help improve signal even in these non-ideal geometries, although so far, no systematic study of the effect and limits of roughness on halide perovskite EBSD patterns has been conducted.

As in standard SEM imaging, the sample surface for EBSD has to be conductive enough to avoid charging effects, especially when a thin-film sample is directly deposited on an insulating substrate such as glass. A gold pre-coating on the sample, as is standard for SEM, however, should not be used for EBSD, as it can damage the surface quality and obscure the crystallographic orientation. Simply applying conductive tapes such as copper, gold, or carbon on top of the sample close to but not overlapping with the region of interest (within several millimeters) can help reduce surface charging enough to enable measurements.<sup>[25,27]</sup> An alternative approach is to use low pressure of water vapor,<sup>[61]</sup> which can help to increase surface conductivity of the sample without influencing the quality of its diffraction pattern.

### 3.3. Beam Damage

Standard EBSD is known to damage soft-materials such as halide perovskites. Using cryogenic SEM can improve critical dose to 12 e<sup>-</sup> Å<sup>-2</sup> for CH<sub>3</sub>NH<sub>3</sub>PbI<sub>3</sub> and 46 e<sup>-</sup> Å<sup>-2</sup> CH<sub>3</sub>NH<sub>3</sub>PbBr<sub>3</sub>. These values are proven to be four times higher than the maximal dose at room temperature.<sup>[14,62,63]</sup> This critical limit is also related to the composition, and therefore decomposition route of the perovskite. Inorganic halide perovskites such as Cs<sub>2</sub>BiAgBr<sub>6</sub> are reported to have a higher resistance to the electron beam.<sup>[64]</sup> While there was no direct measurement of beam sensitivity in CsPbBr<sub>3</sub>, the high quality spot and mapping results collected on standard commercial EBSD systems suggest that it is much more stable under the electron beam than the organic–inorganic hybrid lead halide perovskites.<sup>[60,65]</sup> For successful mapping rather than a point survey, the hybrid halide perovskites require a dose <0.1 e<sup>-</sup> Å<sup>-2</sup>.<sup>[27,57,66–68]</sup> Accelerating voltage is a key parameter for damage in halide perovskites. This value varies from 10 to 20 kV in the literature,<sup>[60,69]</sup> except for one work using 5 kV with a Timepix detector.<sup>[26]</sup> Besides voltage, other parameters that could be important for reducing damage while acquiring high quality EBSD patterns, such as beam current, dwell time, step size, and vacuum level are rarely listed in literature. We suggest that future publications report these values, so that even without a systematic study of the effect of such parameters, some indication of the useable range of values can be determined. Other methods for reducing the effect of beam damage are using thicker films (>1 μm) to increase the interaction volume between sample and electron beam,<sup>[60]</sup> low-vacuum mode<sup>[28]</sup> in the SEM chamber to prevent charging damage, fast raster during scanning, defocusing the beam,<sup>[70]</sup> or using an advanced cryo-system.<sup>[70]</sup> Although it has not yet been explored with halide perovskites, we suspect defocusing the beam could provide a large improvement, comparable to what has already been observed on ice samples. Due to high beam damage, most EBSD studies in halide perovskite samples to date have been conducted using single spot measurements to compare crystal orientation in a few places of a film, for example, to prove that those spots correspond to the same or different crystallographic orientation.<sup>[64,65,71–73]</sup> However, recent breakthroughs in detector sensitivity, as well as the application of low-vacuum EBSD, have now enabled standard EBSD mapping for halide perovskite thin films.<sup>[25–28,60,74,75]</sup> As will be discussed later, this dramatically increases the potential of the technique, as it opens up the possibility for correlating

crystallographic properties with chemical, electrical, or optical properties and even device performance.

#### 4. EBSD for Perovskites

Relatively few EBSD studies have been conducted on halide perovskite materials due to the substantial damage typically induced by the electron beam. The first example came only in 2016, where single spot measurements in several places along a  $\text{CH}_3\text{NH}_3\text{PbBr}_3$  microplate showed the same crystallographic orientation, which supported the hypothesis that the highly faceted microplates were single crystalline. However, spot measurements of other microplates showed that grain boundaries could also exist even in nicely faceted crystals, suggesting that mapping and not only single spot measurements must be used to verify the crystallinity (Figure 4a,b).<sup>[65]</sup> In 2017, the first halide perovskite EBSD map was demonstrated using large single crystals of the much more e-beam stable  $\text{CsPbBr}_3$  material.<sup>[60]</sup> They showed beautifully uniform orientation and inverse pole figure maps, as would be expected for single crystalline materials. However, it is interesting to note that again the Kikuchi patterns were quite clear despite the substantial surface roughness of the crystals (Figure 4c,d). In 2018, EBSD was also used to show that single crystalline films of  $\text{CH}_3\text{NH}_3\text{PbI}_3$  could be grown epitaxially on KCl single crystals using a simple solution

spin-coating process. The Kikuchi pattern of the  $\text{CH}_3\text{NH}_3\text{PbI}_3$  film was compared to a region of the KCl not covered by the perovskite film to prove the epitaxial relationship (Figure 4e,f). Interestingly, the simulated EBSD pole figures suggest that (110)  $\text{CH}_3\text{NH}_3\text{PbI}_3$  grows epitaxially from (001) KCl single crystals. The authors mention mapping, although no EBSD maps are shown and little detail is provided about the measurements.<sup>[74]</sup> Another attempt of single spot EBSD was used to study grain orientation effects of  $\text{CH}_3\text{NH}_3\text{PbI}_3$  films. Again, sample damage by the electron beam extremely reduced the clarity of their Kikuchi patterns.<sup>[69]</sup>

Further attempts for EBSD mapping came after 2018<sup>[25,28,75,76]</sup> using archetypical  $\text{CH}_3\text{NH}_3\text{PbBr}_3$  and  $\text{CH}_3\text{NH}_3\text{PbI}_3$  thin-films as a model system. One study used low-vacuum SEM which led to substantially less damage under standard EBSD beam currents due to a reduction in surface charging.<sup>[28]</sup> This approach allowed for the first maps of the most widely studied halide perovskite material (Figure 5a). The (110) crystal facets of  $\text{CH}_3\text{NH}_3\text{PbI}_3$  were associated with ferroelectric polarization according to correlated piezo-response force microscopy maps. This first example already showed the power of correlating EBSD mapping with other characterization techniques. The second example<sup>[73,76]</sup> shows much better-quality mapping, perhaps because they used a sample with a much larger average grain size (48  $\mu\text{m}$  vs sub-microns in the earlier case, Figure 5b). However, details on their diffraction pattern quality and setup is yet to be disclosed. All

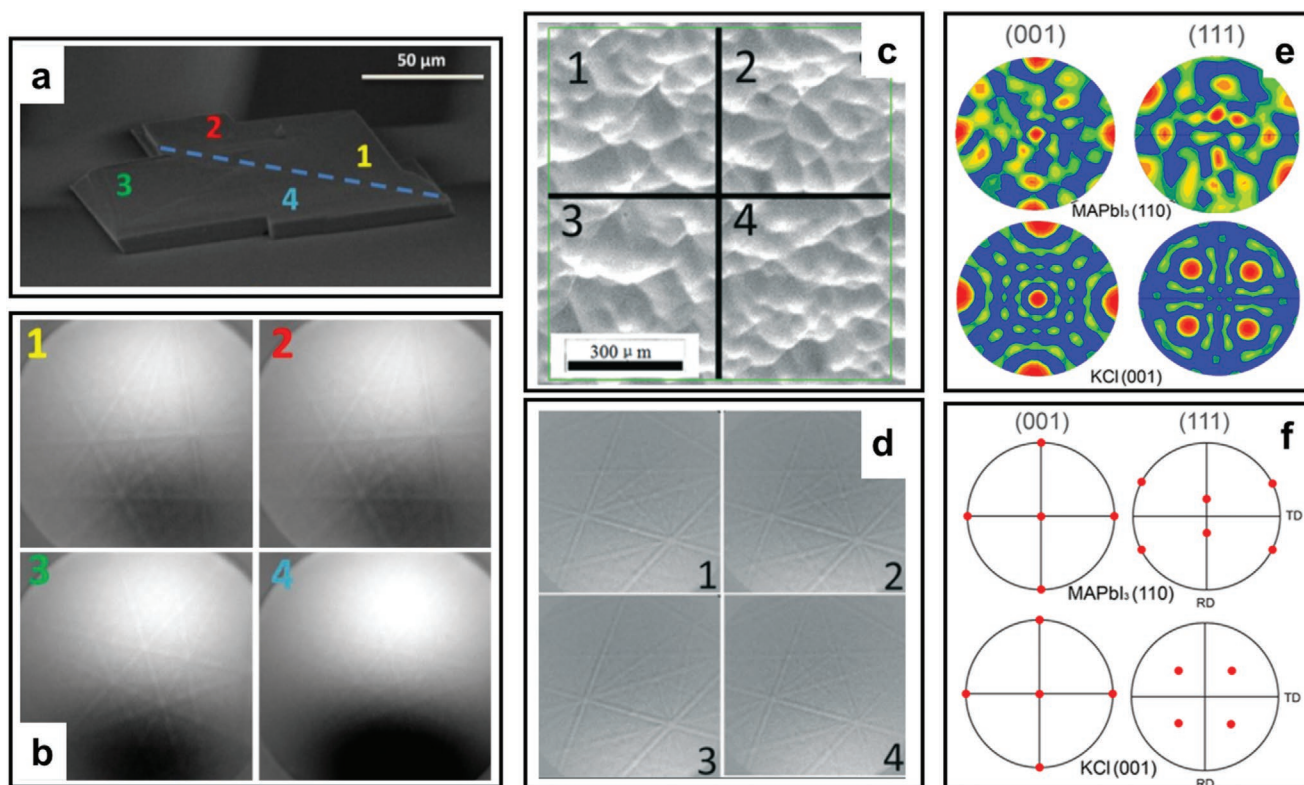


**Figure 4.** EBSD measurement spots on halide perovskites. a)  $\text{CH}_3\text{NH}_3\text{PbBr}_3$  microplate with b) its corresponding EBSD survey spots showing different Kikuchi patterns could exist even in nicely faceted crystals. Reproduced with permission.<sup>[65]</sup> Copyright 2016, American Chemical Society. c)  $\text{CsPbBr}_3$  crystal with d) its corresponding EBSD survey spots showing same Kikuchi patterns despite having rough surfaces. Reproduced with permission.<sup>[60]</sup> Copyright 2017, Royal Society of Chemistry, and e,f)  $\text{CH}_3\text{NH}_3\text{PbI}_3$  thin-film demonstrating an agreement between experimental (e) and simulated (f) pole figures that suggest epitaxial growth of  $\text{CH}_3\text{NH}_3\text{PbI}_3$  on KCl. Reproduced with permission.<sup>[74]</sup> Copyright 2018, American Chemical Society.

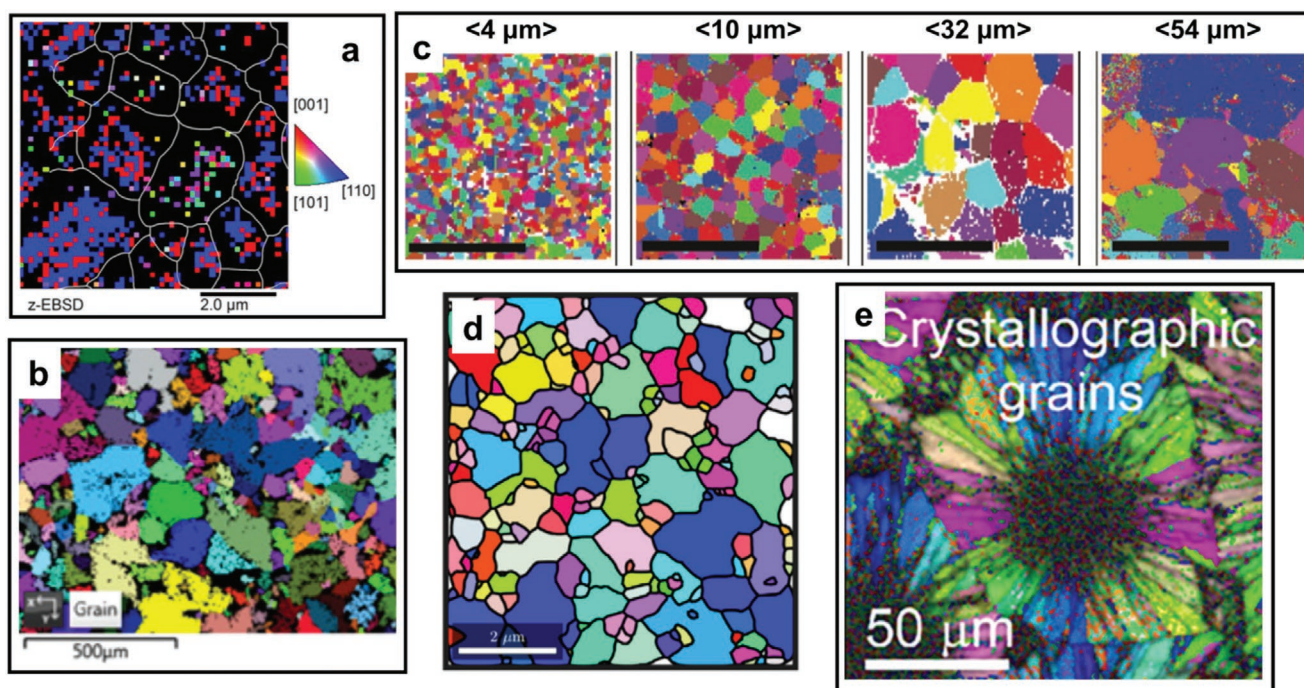


**Figure 5.** EBSD mapping on halide perovskites. a)  $\text{CH}_3\text{NH}_3\text{PbI}_3$  thin-film using a low-vacuum SEM setup. Reproduced with permission.<sup>[28]</sup> Copyright 2019, Wiley, b)  $\text{CH}_3\text{NH}_3\text{PbI}_3$  thin-film featuring much larger grain sizes. Reproduced with permission.<sup>[76]</sup> Copyright 2019, Oxford Instruments, c)  $\text{CH}_3\text{NH}_3\text{PbBr}_3$  thin-film with average grain sizes ranging from 4 to 54  $\mu\text{m}$ . Reproduced with permission.<sup>[25]</sup> Copyright 2018, Wiley, d)  $\text{CH}_3\text{NH}_3\text{PbI}_3$  thin-film having similar grain sizes with (a), but taken using different EBSD detectors. Reproduced with permission.<sup>[27]</sup> Copyright 2019, Cell Press, and e)  $\text{CH}_3\text{NH}_3\text{PbI}_3$  thin-film having  $\approx 50 \mu\text{m}$  spherulitic grain faceted structures. Reproduced with permission.<sup>[26]</sup> Copyright 2019, American Chemical Society. Figures (c)–(e) were obtained using newly developed direct electron detector.

of these measurements were still conducted on standard commercial EBSD systems using a phosphor screen and camera. In early 2018,<sup>[25]</sup> a highly sensitive solid-state detector was introduced for the purpose of EBSD mapping on halide perovskite thin-films where a set of thin-film samples of  $\text{CH}_3\text{NH}_3\text{PbBr}_3$  each having different grain sizes from 4 to 54  $\mu\text{m}$  was tested (Figure 5c). Likewise, using the same detector and setup, successful EBSD mappings were done on archetypical sub-micron grains of  $\text{CH}_3\text{NH}_3\text{PbI}_3$  typically used in high efficiency solar cells<sup>[27]</sup> (Figure 5d), as well as in a similar system having  $\approx 50 \mu\text{m}$  spherulitic grain faceted structures<sup>[26]</sup> (Figure 5e). The results of EBSD mapping can help to dispel some misconceptions about grain boundary characteristics, including grain sizes, distribution, orientation, and their effects on optoelectronics properties and device performance. In the following, we pinpoint what we have learned from the results of EBSD mapping.

## 5. What Have We Learned about Halide Perovskites from EBSD Mapping?

### 5.1. SEM Images Cannot Provide Accurate Information about Grain Boundaries

SEM images do not provide any crystallographic information, so they also cannot accurately identify grain boundaries. Although in some cases the apparent “grain” sizes from SEM is consistent with the actual grain sizes obtained by EBSD,

especially for films having large grains ( $>10 \mu\text{m}$ ), SEM contrast can also be very deceiving. For example, Adhyaksa et al. highlighted specific cases where SEM contrast suggested a grain boundary where there was none and where SEM contrast was smooth even though EBSD showed a clear grain boundary<sup>[25]</sup> (Figure 6a,b). Even more striking examples have been shown for  $\text{CH}_3\text{NH}_3\text{PbI}_3$  produced by the flash infrared annealing (FIRA) method.<sup>[26]</sup> In that case, EBSD gave additional valuable information showing the nucleation of wire-like crystallites led to film formation (Figure 6c). These studies verify that that when reporting claims on the effect of grain boundaries, suitable crystallographic tools, such as EBSD, should be used.

### 5.2. Grain Boundaries Can Be Either Detrimental or Beneficial for Optical Properties

By correlating EBSD with measurements of optical and electrical properties, the effect of grain boundaries on carrier lifetime, minority carrier diffusion length, and mobility can be determined. As with previous studies on Si, CdTe, and CIGS have shown, it is important to realize that grain boundaries may have multiple competing effects, leading to net positive or negative results depending on the nature of the grain boundaries as well as the material composition and other correlated defects. So far in the halide perovskites studied, carrier lifetime, minority carrier diffusion length,

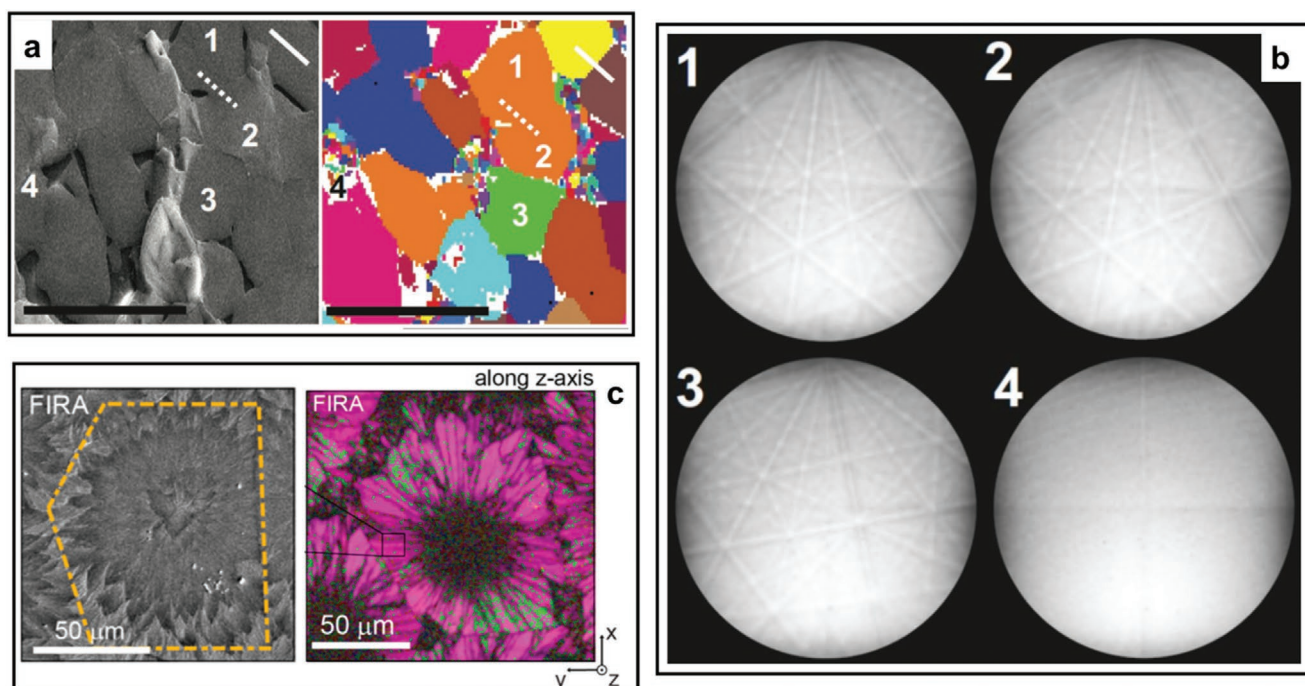


**Figure 6.** EBSD maps compared to SEM images. a)  $\text{CH}_3\text{NH}_3\text{PbBr}_3$  with b) its corresponding Kikuchi patterns on different spots indicating features from SEM can be deceiving where the apparent boundary between crystal 1 and 2 is actually not a real grain boundary based on EBSD (both having same Kikuchi patterns). Conversely, on the surface that appears smooth in SEM (across the solid white line), there is a real grain boundary (from EBSD). Even more striking, there is lack of crystallographic information (no Kikuchi pattern) in crystal 4, which indicates crystallographic disorder (amorphous phase). Reproduced with permission.<sup>[25]</sup> Copyright 2018, Wiley. c)  $\text{CH}_3\text{NH}_3\text{PbI}_3$  fabricated by flash infrared annealing (FIRA) method where the EBSD map shows more detailed information about nucleation of wire-like crystallites that led to film formation. Reproduced with permission.<sup>[26]</sup> Copyright 2019, American Chemical Society. Both examples show clearly that SEM cannot provide accurate information about grain boundaries.

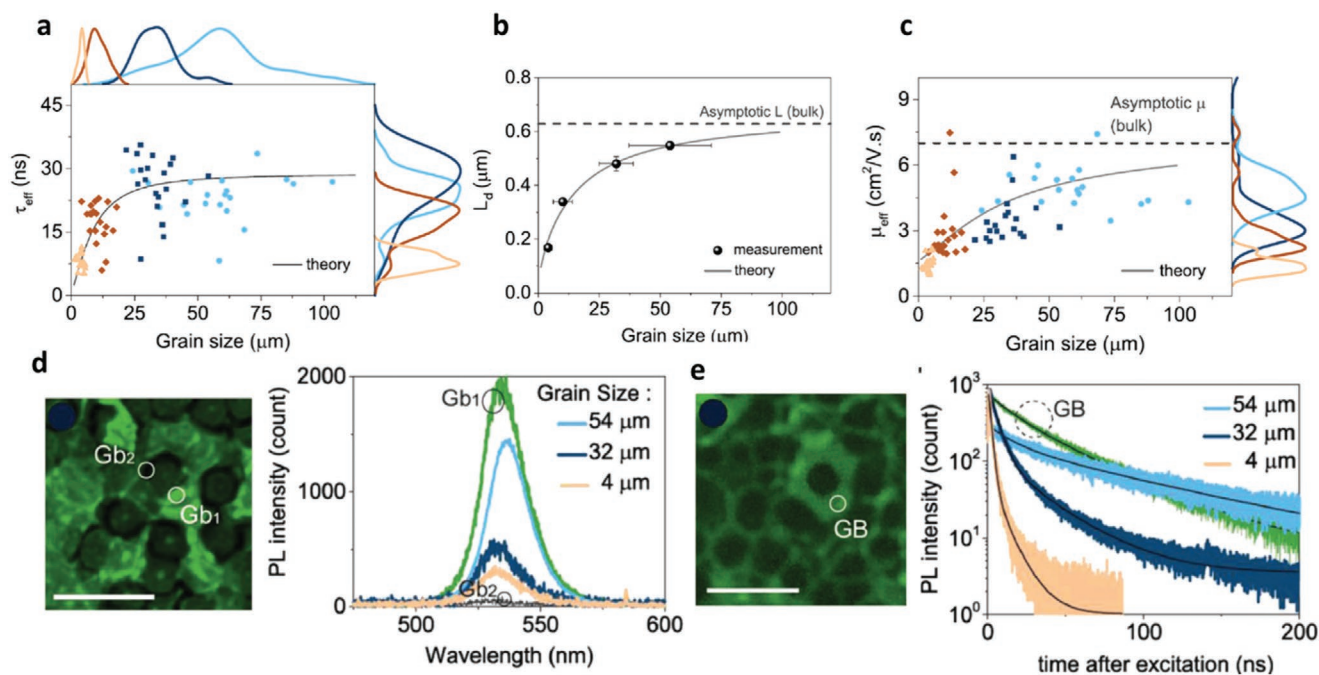


**Figure 7.** The relation between grain size and optoelectronic properties of  $\text{CH}_3\text{NH}_3\text{PbBr}_3$  perovskite. a) carrier lifetime, b) minority carrier diffusion length, and c) carrier mobility versus grain size. d) PL intensity map and several spectra of typical results from films with different grain size compared to several specific locations. e) Lifetime map and time-resolved PL decay traces of typical results from films with different grain size compared to the location with amorphous material between grains. Reproduced with permission.<sup>[25]</sup> Copyright 2018, Wiley.

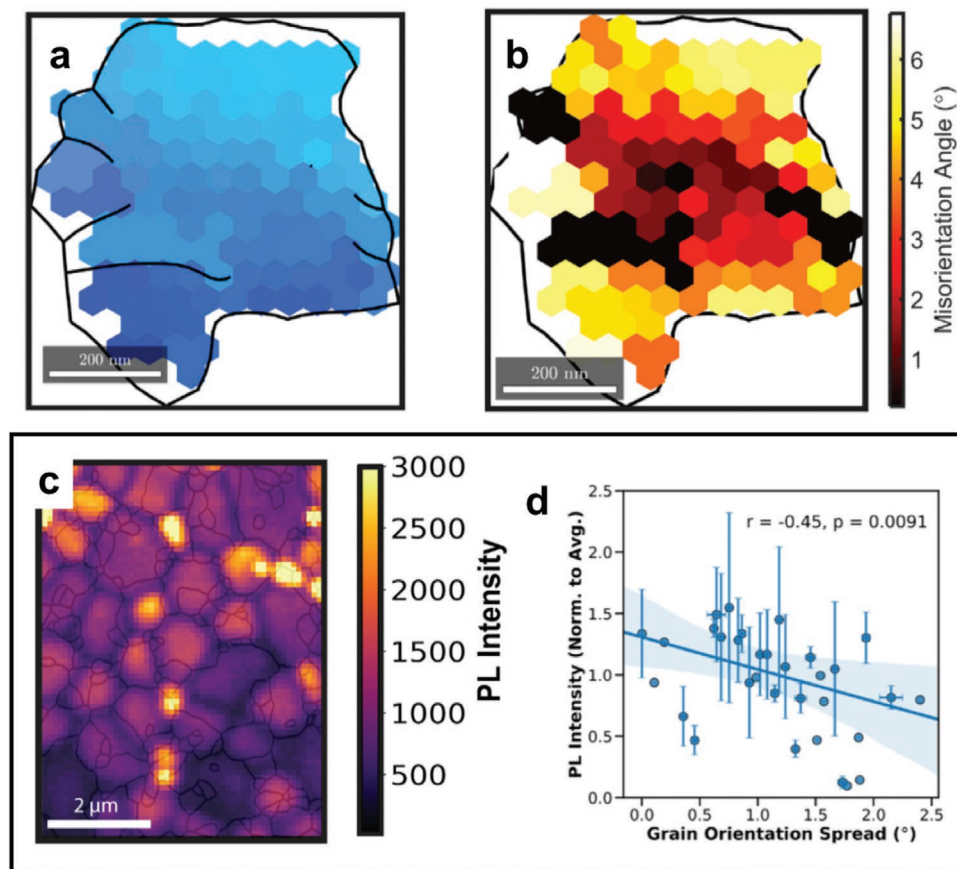


**Figure 8.** Correlating EBSD and PL maps.<sup>[27]</sup> a) EBSD map showing co-existence of outer grain boundaries (boundary with other grains), and sub-grain boundary within the individual grain on  $\text{CH}_3\text{NH}_3\text{PbI}_3$  thin-film, and b) its average pixel-to-pixel misorientation demonstrating a local crystallographic heterogeneity in the grain. c) Confocal PL map overlapped with grain boundary network obtained from EBSD in  $\text{CH}_3\text{NH}_3\text{PbI}_3$ , and d) its statistical plot of PL intensity as a function of grain orientation spread showing a negative correlation that indicates local crystallographic heterogeneity may induce a higher non-radiative recombination loss. Reproduced with permission.<sup>[27]</sup> Copyright 2019, Cell Press.

and mobility are generally better with larger grain sizes up to 60  $\mu\text{m}$  (Figure 7a–c). While in most cases the grain boundaries are well-defined interfaces, special cases with amorphous material located between grains has been observed to lead to unusual behavior. For example, while the sharp crystalline boundaries lead to the expected lower photoluminescence intensity and shorter lifetime compared to the grain interior, the amorphous regions at grain boundaries have stronger photoluminescence and longer carrier lifetime than the grain interior (Figure 7d,e).<sup>[25]</sup> Although the exact mechanism is still under investigation, this unusual behavior likely arises from a combination of improved surface/grain boundary passivation and improved material quality (e.g., by defect gettering from the grains into the amorphous regions), while differences in light outcoupling or reabsorption may also contribute. It is also possible that other correlated defects such as point defects (vacancies, anti-sites, interstitials), dislocations, strain, or compositional variations play an important role. These results show the importance of not only looking at grain size, but also the nature of the grain boundary as well as any other local properties that can be measured, for coming to a full understanding of the underlying mechanism.

### 5.3. Sub-Grain Boundaries Can Increase Non-Radiative Recombination

Grain boundaries in halide perovskites sometime can protrude within the grain interior in addition to forming at the exterior. These are known as sub-grain boundaries, and SEM images definitely cannot identify such missing information (Figure 8a,b). This important feature was found to be anti-correlated with the resulting photoluminescence intensity, indicating a detrimental effect (possibly due to local strain) of the sub-grain boundaries in  $\text{CH}_3\text{NH}_3\text{PbI}_3$  (Figure 8c,d).<sup>[27]</sup> It is, however, interesting to find out whether such sub-grain boundaries can also be more important than the exterior grain boundaries. Twinning, a crystallographic mirror within a grain, can also be considered a sub-grain boundary. While its presence in  $\text{CH}_3\text{NH}_3\text{PbI}_3$  was observed in TEM,<sup>[77]</sup> its effect on local photoluminescence is yet to be known.

### 5.4. Distribution Can Be More Important than Average Misorientation and Grain Sizes

Increased average grain size usually comes at the cost of having larger grain size distribution<sup>[25]</sup> and local heterogeneity.<sup>[27]</sup>

This may be why enlarging the grain size in  $\text{CH}_3\text{NH}_3\text{PbI}_3$  is not always correlated with better optoelectronic properties and device performance. The distribution of grain sizes could be the limiting factor affecting the microscopic properties of the films. Likewise, for crystal orientation, minimizing misorientation within and among the grains can likely help to suppress local stress associated with non-radiative recombination of the films.<sup>[57,78]</sup> However, it still is not clear if there are specific crystal orientations or a combined orientation favorable for enhancing the optoelectronic properties of the halide perovskite films, or if certain grain boundary orientations are particularly detrimental. Part of the difficulty is disentangling many potentially interrelated contributing factors such as point defects, dislocations, grain boundaries, stress, and compositional variations, particularly in the state-of-the-art films with very complex mixtures of elements. Correlative studies using EBSD, photoluminescence microscopy,<sup>[27]</sup> cathodoluminescence,<sup>[79]</sup> conductive atomic force microscopy<sup>[28]</sup> or Raman,<sup>[80]</sup> and the use of machine learning may help to understand further this complex problem.<sup>[81]</sup> However, note that EBSD may not represent the entire bulk crystallographic misorientation, unless there is no other grain underneath the top grains. One should incorporate the distribution of grain sizes on top of merely average grain size in order to study the effect of grain boundaries or sizes, for instance, through device modeling.<sup>[25]</sup> By plugging this distribution of crystal misorientation into device modeling, we will understand that our common intuition can be quite misleading.

## 6. Limitation, Current Development, and Future of EBSD

The core success of EBSD technique in halide perovskites depends on both instrumentation and software development. We point out some key developments on state-of-the-art topology of the detectors, and briefly some advanced algorithms applied for diffraction pattern recognition, what limits those, and future they may bring through in situ characterization.

### 6.1. Introducing a New Era of Direct Electron Detector

The emergence of a direct-electron detector has benefited a variety of fields and applications, including high-energy particle physics and medical imaging. One famous example is the discovery of the elusive Higgs boson particle. Arguably, the key success of the discovery relies on an advanced topology within the detector.<sup>[82,83]</sup> However, for some reason, state-of-the-art commercial EBSD detectors failed to follow this trend.

All commercially available EBSD detectors are based on charge integrating sensors such as CCD (charge-couple device), CMOS (complementary metal-oxide-semiconductor), phosphorous screen/camera, or a combination thereof.<sup>[84,85]</sup> Those detectors in combination with a fast data acquisition work well at relatively high dose, but show insufficient performance when it comes to imaging sensitive materials such as halide perovskites. It is not surprising because the detector system undergoes two conversion processes from electron-to-photon (phosphorous screen), then back again from photon-to-electron

(CCD), along with inevitable efficiency losses (parasitic absorption and scattering) along the way.

By completely working on a noise free detector system (removing the dependency on dark current) would in principle solve the aforementioned problem. This can be achieved by designing a direct electron detector system where the sensor is decoupled from the electronics. Hence, the electronic topology can be easily modified to always work above the noise floor. Originally developed for mass spectroscopy at AMOLF, this new direct electron detector is currently being pursued in collaboration with Nikhef and CERN.<sup>[84,86]</sup> This detector is based on a single particle counting system. The counting system carries very important information that is time stamping (time-over-threshold and time-of-arrival). This time tagging capability, if designed properly, can have a resolution down to sub-ns which opens up any time-resolved characterization technique involving an electron beam. Although the readout rate from this detector is still limited by a bandwidth of a standard computer network, the acquisition process is not logistically data demanding. Perhaps, the most important development for the detector in the future will be on improving its time tagging capability, which standard detectors do not have. This dynamic space and time capability of the detector can have a profound impact, for example, on detailed monitoring of grain boundary growth or shrinkage through the microstructural network in very sensitive materials, such as halide-perovskites.

### 6.2. Advanced Pattern Analysis

All advanced algorithms currently applied for EBSD will further benefit the halide perovskite community. One notable example is the algorithm for high angular resolution EBSD (HR-EBSD) popularized by Wilkinson et al.<sup>[24,87]</sup> using a cross-correlation technique (Figure 9a). This can increase the overall resolution of a map ( $\approx 10^{-4}$  rad lattice distortion, which is  $\approx 1000$  times higher angular resolution compared to conventional EBSD). This is useful, for example, in mapping sub-micron grain sizes of archetypical  $\text{CH}_3\text{NH}_3\text{PbI}_3$  perovskites typically used in solar cells. The cross-correlation method in HR-EBSD also relaxes the dependence on an initial reference or simulated Kikuchi pattern, which requires a known measurement geometry and aberration correction. Overall, the HR-EBSD may improve the confidence interval on distribution mapping of sub-grain boundaries, relative stress, or twinning defects, which is quite challenging if only related to the standard Hough/Radon transform algorithms (Figure 9b,c).<sup>[88–90]</sup>

Sub-micron grains of  $\text{CH}_3\text{NH}_3\text{PbI}_3$  often consist of multiple decomposed phases (tetragonal, cubic, orthorhombic) having similar lattice constant.<sup>[91]</sup> This is problematic for EBSD mapping because EBSD typically is not used to determine the lattice constant. While the symmetry of the Kikuchi pattern can be used to identify the crystallographic phase, when two phases have a symmetry difference that arises from a very small distortion in the lattice constant along one or more axes, definitive identification may be impossible with conventional EBSD systems. However, more recently the combination of very high angular resolution and careful calibration of all distortions in the detection system have allowed for tiny strains and small

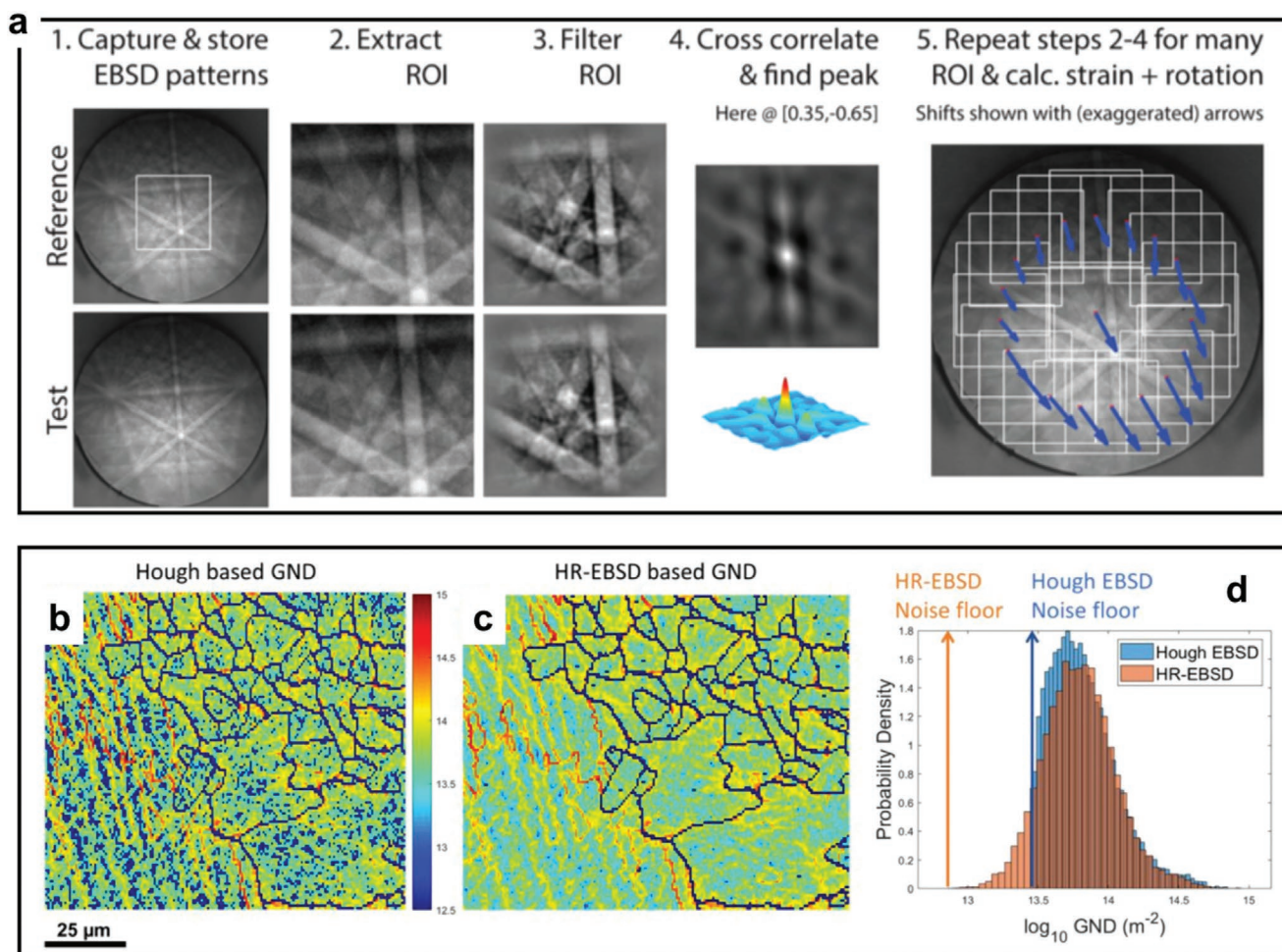


**Figure 9.** High-resolution EBSD. a) Routine procedure to perform high-resolution EBSD analysis (HR-EBSD). Steps 1 to 5 are repeated over several “Test” pixels to generate strain and rotation maps. Reproduced with permission.<sup>[87]</sup> Copyright 2013, Cambridge University Press. Comparison between conventional Hough transform approach (b) versus HR-EBSD (c). d) Histogram of geometrically necessary dislocation (GND) density between Hough and HR-EBSD showing a lower noise floor using HR-EBSD, therefore a better angular resolution. Reproduced with permission.<sup>[90]</sup> Copyright 2020, Elsevier.

differences in lattice constant to be detected.<sup>[92,93]</sup> An additional complication is that halide perovskites with larger grains, such as  $\text{CH}_3\text{NH}_3\text{PbBr}_3$ , can be very rough, which can degrade the quality of collected diffraction patterns. Given advances in development of the algorithms for image correlation and pattern analysis, we believe these issues can be solved, perhaps, through a correlative study to gain better confidence of analysis. Information obtained from such cross-correlated EBSD is relative to a reference, so it is often helpful to map the same region-of-interest with other techniques such as micro-Raman, nano-indenter, transmission electron microscopy, for instance to calibrate local strains.

Halide perovskite thin films are very sensitive to the dose of an electron beam. An algorithm that can capture the degradation dynamics of the crystal phase (given the detector itself is sensitive enough) will provide another level of understanding, not only spatially but also toward various timescales, of grain boundary degradation. Given the very large initial data set that is to be expected during this acquisition process, and also demand for accurate predictions involving change of the crystal phases, interpolation techniques such as machine

learning will be extremely useful in the future for every EBSD software.

### 6.3. In Situ Correlation Studies Using EBSD

The composition of halide perovskite materials in state-of-the-art devices is very complex involving multiorganic and inorganic cations, alloys/mixtures of halides, and dynamic ion migration.<sup>[94]</sup> On top of that, many characterization probes (electron/ion beams, lasers, temperature, pressure) can dramatically alter such properties.<sup>[95]</sup> Such changes can easily modify defect formation energies, position of energy alignment, ionic diffusion constants, local field-assisted mobilities, reactivity with moisture/oxygen, surface recombination, local strain and distribution, interfacial surface energies, doping level, electron–phonon coupling, and crystallinity or nature at the grain boundaries.<sup>[25,57,78,96–98]</sup> In situ characterization using EBSD under external perturbations (illumination, electric field gradients, elevated temperature, and environmental exposure) will provide a complete and

rational picture on the impact of local crystal misorientation of the materials with those dynamic variables that may change device performance.

This in situ characterization can be done, for instance, by using a carefully designed sample stage having an active temperature controller connected to an electronic interface that also allows for electrical biasing. Designing a compartment to enable local environmental exposure (pressure, moisture/oxygen, and illumination) is relatively challenging. However, a similar idea adopted for cryogenic electron microscopy can be applied.<sup>[99,100]</sup> Monitoring the dynamics at grain boundaries under elevated temperature will provide valuable insights on how the seeds crystalize, grow, and transform to different phases (e.g., in the case of CH<sub>3</sub>NH<sub>3</sub>PbI<sub>3</sub> tetragonal to orthorhombic or to cubic at lower or higher temperature, respectively). This complex information can also be connected to electrical bias (e.g., EBIC) to monitor the local diffusion and collection of charges across and within the grain boundaries. We believe such aggregates will help understand in more detail various physical phenomena in looking at grain boundaries, not only as a local system, but now as an entire network. A concept of correlated disorder at the grain boundaries for charge diffusion perhaps can open a completely new horizon between preferentially small and large grain sizes for high-efficiency solar cells.

## 7. Conclusion

EBSM is a very powerful technique for halide perovskites and yet it has been highly underutilized in the community. Recent advances on the EBSM detector and low vacuum measurement technique have now overcome the damage threshold of these sensitive materials under the electron beam. We encourage researchers in the community to exploit and carefully study the effect of micro-structural arrangement of polycrystalline grains in halide perovskites, and correlate it with other thin-film properties (optical, electrical, mechanical, and chemical) relevant for device applications, in addition to specifically reporting detailed parameters used for successful measurements (accelerating voltage, beam current, dwell time, step size, vacuum level). In principle, EBSM can help to do this correlation study at a “pixel-by-pixel” level. Aggregates of such studies will help us to dispel common misconceptions about grain boundaries in halide perovskites as highlighted in this review, and can point the way forward to accelerate the development for better materials and their applications.

## Acknowledgements

E.C.G. and H.S. were supported by the Dutch Science Foundation (NWO) through the Joint Solar Program III. E.C.G. and G.W.P.A. received funding from the European Research Council grant no. 337328 “NanoEnabledPV.”

## Conflict of Interest

The authors declare no conflict of interest.

## Keywords

crystallography, electron backscatter diffraction, grain boundaries, halide perovskites, orientation mapping, solar cells

Received: January 28, 2020

Revised: April 3, 2020

Published online:

- [1] H. L. Wells, *Am. J. Sci* **1893**, s3–45, 121.
- [2] G. E. Eperon, M. T. Horantner, H. J. Snaith, *Nat. Rev. Chem.* **2017**, 1, 0095.
- [3] Z. Li, T. R. Klein, D. H. Kim, M. J. Yang, J. J. Berry, M. F. A. M. van Hest, K. Zhu, *Nat. Rev. Mater.* **2018**, 3, 18017.
- [4] J. P. Correa-Baena, M. Saliba, T. Buonassisi, M. Gratzel, A. Abate, W. Tress, A. Hagfeldt, *Science* **2017**, 358, 739.
- [5] H. J. Snaith, P. Hacke, *Nat. Energy* **2018**, 3, 459.
- [6] Y. H. Deng, X. P. Zheng, Y. Bai, Q. Wang, J. J. Zhao, J. S. Huang, *Nat. Energy* **2018**, 3, 560.
- [7] M. A. Green, A. Ho-Baillie, *ACS Energy Lett.* **2017**, 2, 822.
- [8] C. X. Xiao, Z. Li, H. Guthrey, J. Moseley, Y. Yang, S. Wozny, H. Moutinho, B. To, J. J. Berry, B. Gorman, Y. F. Yan, K. Zhu, M. Al-Jassim, *J. Phys. Chem. C* **2015**, 119, 26904.
- [9] S. Y. Sun, T. Salim, N. Mathews, M. Duchamp, C. Boothroyd, G. C. Xing, T. C. Sum, Y. M. Lam, *Energy Environ. Sci.* **2014**, 7, 399.
- [10] D. Nanova, A. K. Kast, M. Pfannmoller, C. Muller, L. Veith, I. Wacker, M. Agari, W. Hermes, P. Erk, W. Kowalsky, R. R. Schroder, R. Lovrincic, *Nano Lett.* **2014**, 14, 2735.
- [11] Q. Jeangros, M. Duchamp, J. Werner, M. Kruth, R. E. Dunin-Borkowski, B. Niesen, C. Ballif, A. Hessler-Wyser, *Nano Lett.* **2016**, 16, 7013.
- [12] F. Qin, Z. Wang, Z. L. Wang, *ACS Nano* **2016**, 10, 9787.
- [13] G. Divitini, S. Cacovich, F. Matteocci, L. Cina, A. Di Carlo, C. Ducati, *Nat. Energy* **2016**, 1, 15012.
- [14] Y. B. Li, W. J. Zhou, Y. Z. Li, W. X. Huang, Z. W. Zhang, G. X. Chen, H. S. Wang, G. H. Wu, N. Rolston, R. Vila, W. Chiu, Y. Cui, *Joule* **2019**, 3, 2854.
- [15] J. P. Correa-Baena, Y. Luo, T. M. Brenner, J. Snaider, S. Sun, X. Li, M. A. Jensen, N. T. P. Hartono, L. Nienhaus, S. Wiegold, J. R. Poindexter, S. Wang, Y. S. Meng, T. Wang, B. Lai, M. V. Holt, Z. Cai, M. G. Bawendi, L. Huang, T. Buonassisi, D. P. Fenning, *Science* **2019**, 363, 627.
- [16] X. Y. Li, Y. Q. Luo, M. V. Holt, Z. H. Cai, D. P. Fenning, *Chem. Mater.* **2019**, 31, 2778.
- [17] Y. L. Chang, P. Y. Chen, Y. T. Tsai, J. R. Yang, *Mater. Charact.* **2016**, 113, 17.
- [18] M. Herbig, M. Kuzmina, C. Haase, R. K. W. Marceau, I. Gutierrez-Urrutia, D. Haley, D. A. Molodov, P. Choi, D. Raabe, *Acta Mater.* **2015**, 83, 37.
- [19] T. Tanaka, A. J. Wilkinson, *Microsc. Microanal.* **2018**, 24, 962.
- [20] L. E. Watt, P. A. Bland, D. J. Prior, S. S. Russell, *Meteorit. Planet. Sci.* **2006**, 41, 989.
- [21] D. J. Prior, E. Mariani, J. Wheeler, in *Electron Backscatter Diffraction in Materials Science*, Springer, New York **2009**, p. 345.
- [22] B. L. Adams, S. I. Wright, K. Kunze, *Metall. Trans. A* **1993**, 24, 819.
- [23] J. R. Michael, R. P. Goehner, presented at the *Annual Meeting of the Electron Microscopy Society of America*, Cincinnati, OH 1–6 August **1993**.
- [24] A. J. Wilkinson, T. B. Britton, *Mater. Today* **2012**, 15, 366.
- [25] G. W. P. Adhyaksa, S. Brittman, H. Abolins, A. Lof, X. Li, J. D. Keelor, Y. Luo, T. Duevski, R. M. A. Heeren, S. R. Ellis, D. P. Fenning, E. C. Garnett, *Adv. Mater.* **2018**, 30, 1804792.

- [26] L. A. Muscarella, E. M. Hutter, S. Sanchez, C. D. Dieleman, T. J. Savenije, A. Hagfeldt, M. Saliba, B. Ehrler, *J. Phys. Chem. Lett.* **2019**, *10*, 6010.
- [27] S. Jariwala, H. Y. Sun, G. W. P. Adhyaksa, A. Lof, L. A. Muscarella, B. Ehrler, E. C. Garnett, D. S. Ginger, *Joule* **2019**, *3*, 3048.
- [28] T. Leonhard, A. D. Schulz, H. Rohm, S. Wagner, F. J. Altermann, W. Rheinheimer, M. J. Hoffmann, A. Colsmann, *Energy Technol.* **2019**, *7*, 1800989.
- [29] S. H. O. J. I. Nishikawa, S. E. I. S. H. I. Kikuchi, *Nature* **1928**, *122*, 726.
- [30] M. V. Laue, *Ann. Phys.* **1935**, *415*, 705.
- [31] M. N. Alam, M. Blackman, D. W. Pashley, *Proc. R. Soc. London, Ser. A* **1954**, *221*, 224.
- [32] J. A. Venables, C. J. Harland, *Philos. Mag.* **1973**, *27*, 1193.
- [33] D. J. Dingley, K. Baba Kishi, presented at *Proc. of the XIth Int. Congress on Electron Microscopy*, Kyoto, Japan August–September **1986**.
- [34] S. I. Wright, B. L. Adams, *Metal. Trans. A* **1992**, *23*, 759.
- [35] J. B. Burns, A. R. Hanson, E. M. Riseman, *IEEE Trans. Pattern Anal. Mach. Intell.* **1986**, *8*, 425.
- [36] R. P. Goehner, J. R. Michael, *J. Res. Natl. Inst. Stand. Technol.* **1996**, *101*, 301.
- [37] F. M. A. Hadadzadeha, M. A. Wells, D. L. Chen, *Mater. Sci. Eng., A* **2018**, *709*, 5.
- [38] S. X. Tingguang Liu, B. Zhou, Q. Bai, G. S. Rohrer, *J. Mater. Res.* **2018**, *33*, 13.
- [39] S. Choi, S. Han, Y. N. Lee, *Palaeontology* **2019**, *62*, 777.
- [40] I. Prieto, R. Kozak, O. Skibitzki, M. D. Rossell, P. Zaumseil, G. Capellini, E. Gini, K. Kunze, Y. A. R. Dasilva, R. Erni, T. Schroeder, H. von Kanel, *Nanotechnology* **2017**, *28*, 135701.
- [41] J. B. Marro, C. A. Okoro, Y. S. Obeng, K. C. Richardson, *J. Struct. Geol.* **2017**, *164*, D543.
- [42] S. W. Schmitt, F. Schechtel, D. Amkreutz, M. Bashouti, S. K. Srivastava, B. Hoffmann, C. Dieker, E. Spiecker, B. Rech, S. H. Christiansen, *Nano Lett.* **2012**, *12*, 4050.
- [43] D. J. Prior, K. Lilly, M. Seidemann, M. Vaughan, L. Becroft, R. Easingwood, S. Diebold, R. Obbard, C. Daghljan, I. Baker, T. Caswell, N. Golding, D. Goldsby, W. B. Durham, S. Piazzolo, C. J. L. Wilson, *J. Microsc.* **2015**, *259*, 237.
- [44] C. W. Xue, H. H. Loi, A. Duong, M. Parker, *Phys. Status Solidi (RRL)* **2016**, *10*, 673.
- [45] E. M. Tennyson, J. A. Frantz, J. D. Myers, J. S. Sanghera, R. Y. Bekele, S.-M. Na, M. S. Leite, *2015 IEEE 42nd Photovoltaic Specialist Conf. (PVSC)*, IEEE, Piscataway, NJ **2015**.
- [46] H. Moutinho, J. Moseley, M. Romero, R. Dhere, C.-S. Jiang, K. Jones, J. Duenow, Y. Yan, M. Al-jassim, *2013 IEEE 39th Photovoltaic Specialists Conf. (PVSC)*, IEEE, Piscataway, NJ **2013**.
- [47] J. D. Poplawsky, N. R. Paudel, C. Li, C. M. Parish, D. Leonard, Y. F. Yan, S. J. Pennycook, *Adv. Energy Mater.* **2014**, *4*, 1400454.
- [48] H. Nukala, J. L. Johnson, A. Bhatia, E. A. Lund, W. H. Oo, L. W. Rieth, M. Nowell, M. A. Scarpulla, *MRS Proc.* **2010**, *1268*, 1268-EE03-03.
- [49] H. Moutinho, M. Young, S. Harvey, C.-S. Jiang, C. Perkins, S. Wilson, M. Al-jassim, I. Repins, G. Teeter, *2014 IEEE 40th Photovoltaic Specialist Conf. (PVSC)*, IEEE, Piscataway, NJ **2014**.
- [50] A. Stoffers, O. Cojocaru-Miredin, W. Seifert, S. Zaefferer, S. Riepe, D. Raabe, *Prog. Photovoltaics* **2015**, *23*, 1742.
- [51] M. Kawamura, T. Yamada, N. Suyama, A. Yamada, M. Konagai, *Jpn. J. Appl. Phys.* **2010**, *49*, 062301.
- [52] D. L. Barr, W. L. Brown, *Rev. Sci. Instrum.* **1995**, *66*, 3480.
- [53] B. Fultz, J. M. Howe, *Transmission Electron Microscopy and Diffraction of Materials*, Springer Science & Business Media, Berlin **2012**.
- [54] F. J. Humphreys, *J. Mater. Sci.* **2001**, *36*, 3833.
- [55] D. J. Dingley, G. Meaden, D. J. Dingley, A. P. Day, *IOP Conference Series: Materials Science and Engineering*, IOP, Bristol, UK **2018**.
- [56] N. Brodusch, H. Demers, R. Gauvin, *J. Imaging* **2018**, *4*, 88.
- [57] E. M. Tennyson, T. A. S. Doherty, S. D. Stranks, *Nat. Rev. Mater.* **2019**, *4*, 573.
- [58] K. Abbasi, D. Wang, M. A. Fusella, B. P. Rand, A. Avishai, *Microsc. Microanal.* **2018**, *24*, 420.
- [59] L. Koll, P. Tsipouridis, E. A. Werner, *J. Microsc.* **2011**, *243*, 206.
- [60] M. Zhang, Z. Zheng, Q. Fu, Z. Chen, J. He, S. Zhang, L. Yan, Y. Hu, W. Luo, *CrystEngComm* **2017**, *19*, 6797.
- [61] S. M. Habesch, *Mater. Sci. Technol.* **2000**, *16*, 1393.
- [62] D. Zhang, Y. Zhu, L. Liu, X. Ying, C. E. Hsiung, R. Sougrat, K. Li, Y. Han, *Science* **2018**, *359*, 675.
- [63] A. R. Milosavljevic, W. Huang, S. Sadhu, S. Ptasinska, *Angew. Chem., Int. Ed.* **2016**, *55*, 10083.
- [64] O. A. Lozhkina, A. A. Murashkina, M. S. Elizarov, V. V. Shilovskikh, A. A. Zolotarev, Y. V. Kapitonov, R. Kevorkyants, A. V. Emeline, T. Miyasaka, *Chem. Phys. Lett.* **2018**, *694*, 18.
- [65] P. Khoram, S. Brittman, W. I. Dzik, J. N. H. Reek, E. C. Garnett, *J. Phys. Chem. C* **2016**, *120*, 6475.
- [66] M. U. Rothmann, W. Li, Y. Zhu, A. Liu, Z. L. Ku, U. Bach, J. Etheridge, Y. B. Cheng, *Adv. Mater.* **2018**, *30*, 1800629.
- [67] S. L. Chen, X. W. Zhang, J. J. Zhao, Y. Zhang, G. L. Kong, Q. Li, N. Li, Y. Yu, N. G. Xu, J. M. Zhang, K. H. Liu, Q. Zhao, J. Cao, J. C. Feng, X. Z. Li, J. L. Qi, D. P. Yu, J. Y. Li, P. Gao, *Nat. Commun.* **2018**, *9*, 4807.
- [68] N. Klein-Kedem, D. Cahen, G. Hodes, *Acc. Chem. Res.* **2016**, *49*, 347.
- [69] C. P. Jiang, P. P. Zhang, *J. Appl. Phys.* **2018**, *123*.
- [70] I. Weikusat, D. E. W. DA, G. M. Pennock, M. Hayles, C. T. Schneijdenberg, M. R. Drury, *J. Microsc.* **2011**, *242*, 295.
- [71] C. P. Jiang, P. P. Zhang, *J. Appl. Phys.* **2018**, *123*, 083105.
- [72] S. Nickell, D. Zeidler, *Microsc. Microanal.* **2019**, *25*, 568.
- [73] P. Trimby, A. Bewick, D. Abou-Ras, P. Caprioglio, D. Neher, L. Otter, *Microsc. Microanal.* **2019**, *25*, 2394.
- [74] L. Ji, H. Y. Hsu, J. C. Lee, A. J. Bard, E. T. Yu, *Nano Lett.* **2018**, *18*, 994.
- [75] A. B. Pat Trimby, D. Abou-Ras, P. Caprioglio, D. Neher, L. Otter, *Microsc. Microanal.* **2019**, *25*, 2.
- [76] <https://nano.oxinst.com/campaigns/downloads/ebsd-analysis-of-halide-perovskites-using-symmetry> (accessed: May 2020).
- [77] M. U. Rothmann, W. Li, Y. Zhu, U. Bach, L. Spiccia, J. Etheridge, Y. B. Cheng, *Nat. Commun.* **2017**, *8*, 1.
- [78] T. W. Jones, A. Oshero, M. Alsari, M. Sponseller, B. C. Duck, Y. K. Jung, C. Settens, F. Niroui, R. Brenes, C. V. Stan, Y. Li, M. Abdi-Jalebi, N. Tamura, J. E. Macdonald, M. Burghammer, R. H. Friend, V. Bulovic, A. Walsh, G. J. Wilson, S. Lilliu, S. D. Stranks, *Energy Environ. Sci.* **2019**, *12*, 596.
- [79] G. R. Davies, Q. van den Heuvel, S. Matveev, M. R. Drury, I. L. Chinn, M. U. Gress, *Mineral. Petrol.* **2018**, *112*, 231.
- [80] L. H. Friedman, M. D. Vaudin, S. J. Stranick, G. Stan, Y. B. Gerbig, W. Osborn, R. F. Cook, *Ultramicroscopy* **2016**, *163*, 75.
- [81] T. L. Burnett, P. J. Withers, *Nat. Mater.* **2019**, *18*, 1041.
- [82] T. A. Collaboration, *Science* **2012**, *338*, 7.
- [83] A. C. Jovan Mitrevski, *Nucl. Part. Phys., Proc.* **2016**, *273–275*, 3.
- [84] S. Vespucci, A. Winkelmann, G. Naresh-Kumar, K. P. Mingard, D. Maneuski, P. R. Edwards, A. P. Day, V. O'Shea, C. Trager-Cowan, *Phys. Rev. B* **2015**, *92*, 205301.
- [85] A. Roberts, P. Svihra, A. Al-Refaie, H. Graafsma, J. Kupper, K. Majumdar, K. Mavrokoridis, A. Nomerotski, D. Pennicard, B. Philippou, S. Trippel, C. Touramanis, J. Vann, *J. Instrum.* **2019**, *14*, P06001.
- [86] A. R. Faruqi, G. McMullan, *Nucl. Instrum. Methods Phys. Res. Sec. A* **2018**, *878*, 180.
- [87] I. H. Ben Britton, G. Meaden, D. Dingley, *Microsc. Microanal.* **2013**, *27*, 6.
- [88] D. Wallis, L. N. Hansen, T. B. Britton, A. J. Wilkinson, *J. Geophys. Res.* **2019**, *124*, 6337.

- [89] C. Maurice, R. Fortunier, *J. Microsc.* **2008**, *230*, 520.
- [90] C. Y. Zhu, K. Kaufmann, K. S. Vecchio, *Ultramicroscopy* **2020**, *208*, 112851.
- [91] A. Poglitsch, D. Weber, *J. Chem. Phys.* **1987**, *87*, 6373.
- [92] K. Mingard, A. Day, C. Maurice, P. Quedsted, *Ultramicroscopy* **2011**, *111*, 320.
- [93] S. Suzuki, *JOM* **2013**, *65*, 1254.
- [94] S. Brittman, G. W. P. Adhyaksa, E. C. Garnett, *MRS Commun.* **2015**, *5*, 7.
- [95] R. L. Z. Hoyer, P. Schulz, L. T. Schelhas, A. M. Holder, K. H. Stone, J. D. Perkins, D. Vigil-Fowler, S. Siol, D. O. Scanlon, A. Zakutayev, A. Walsh, I. C. Smith, B. C. Melot, R. C. Kurchin, Y. Wang, J. Shi, F. C. Marques, J. J. Berry, W. Tumas, S. Lany, V. Stevanovic, M. F. Toney, T. Buonassisi, *Chem. Mater.* **2017**, *29*, 1964.
- [96] Z. D. Chu, M. J. Yang, P. Schulz, D. Wu, X. Ma, E. Seifert, L. Y. Sun, X. Q. Li, K. Zhu, K. J. Lai, *Nat. Commun.* **2017**, *8*, 2230.
- [97] A. D. Wright, C. Verdi, R. L. Milot, G. E. Eperon, M. A. Perez-Osorio, H. J. Snaith, F. Giustino, M. B. Johnston, L. M. Herz, *Nat. Commun.* **2016**, *7*, 11755.
- [98] W. H. Li, S. K. Yadavalli, D. Lizarazo-Ferro, M. Chen, Y. Y. Zhou, N. P. Padture, R. Zia, *ACS Energy Lett.* **2018**, *3*, 2669.
- [99] D. J. Prior, K. Lilly, M. Seidemann, M. Vaughan, L. Becroft, R. Easingwood, S. Diebold, R. Obbard, C. Daghlain, I. Baker, T. Caswell, N. Golding, D. Goldsby, W. B. Durham, S. Piazzolo, C. J. Wilson, *J. Microsc.* **2015**, *259*, 237.
- [100] P. Wongpan, D. J. Prior, P. J. Langhorne, K. Lilly, I. J. Smith, *J. Glaciol.* **2018**, *64*, 771.
- [101] G. Nolze, C. Grosse, A. Winkelmann, *J. Appl. Crystallogr.* **2015**, *48*, 1405.